On the Use of Azimuth Cutoff for Sea Surface Wind Speed Retrieval From SAR

Yuting Zhu, Giuseppe Grieco, Jiarong Lin, Marcos Portabella, and Xiaoqing Wang

***Abstract*—The accurate retrieval of sea-surface wind field data is crucial for weather forecasting and climate modeling. Despite this, the complexity of sea surface conditions poses significant challenges for satellite-based synthetic aperture radar (SAR) wind retrieval techniques. This study introduces a Bayesian inversion algorithm that incorporates azimuth cutoff wavelength information—a parameter previously underutilized and highly sensitive to varying wind conditions. We aimed to enhance the accuracy of SAR-derived wind estimations to enable more reliable interpretations of marine atmospheric dynamics. The methodology probabilistically combines SAR data with ancillary meteorological information and optimizes the retrieval process through a cost function that leverages the sensitivity of the azimuth cutoff to changes in wind vector fields. The proposed method was comprehensively validated using Sentinel-1 and Gaofen-3 SAR datasets against buoy measurements and wind estimations from scatterometers. The results demonstrated that the proposed method significantly improved the accuracy of wind speed estimations, especially under low-wind conditions and different sea-state conditions, without substantially increasing the computational burden. Although the wind direction retrieval displayed limited enhancement, the improved accuracy in wind speed estimations provides considerable benefits for operational meteorological applications. These findings suggest that the integration of azimuth cutoff information could be a critical step toward obtaining more accurate and reliable wind field retrievals from SAR data, thereby advancing the field of remote sensing and oceanography.**

***Index Terms*—Azimuth cutoff, Bayesian inversion algorithm, sea-surface, wind retrieval.**

I. Introduction

THE sea-surface wind field is a key parameter in marine environmental studies and serves as a fundamental element in both physical oceanography and marine meteorology. In the field of physical oceanography, the sea-surface wind field is a principal factor in generating ocean waves, currents, and vertical mixing, which contributes to variations in sea level driven by wind amidst numerous dynamic and thermodynamic interactions [1].

Over recent decades, scatterometers have emerged as essential tools for enhancing weather forecasting models by providing daily global wind estimates. Currently, the predominant limitation of numerous scatterometers is their spatial resolution, typically at approximately 20 km. This resolution is considered relatively coarse, especially for detailed marine observations, and poses significant implications for activities in coastal regions [2]. In addition to the mesoscale variations in the sea-surface wind field influenced by topography, sea-land breezes, and convective structures introduce additional complexities. Furthermore, the heightened radar backscatter over land—known as the land contamination effect—can impair wind retrieval capabilities in coastal areas, typically affecting regions within an approximate radius of 20–30 km, although variations may occur based on specific geographical and instrumental conditions [3]. This limitation significantly impacts the broad applicability and utility of scatterometers in marine meteorological research and operations in coastal zones.

Recently, both National Aeronautics and Space Administration/Jet Propulsion Laboratory (NASA/JPL) and the EUMETSAT Ocean and Sea Ice Satellite Application Facility have undertaken efforts to mitigate land contamination in coastal acquisitions. Initiatives include the application of a climatology-based correction derived from SeaWinds onboard QuikSCAT, as well as an empirical method known as "noise-regularization" in studies using the Advanced Scatterometer (ASCAT) onboard the Metop series [4], [5]. Furthermore, certain researchers have implemented empirical corrections for ASCAT acquisitions [6].

The normalized radar cross-section (NRCS) over the ocean is significantly affected by the sea surface wind direction relative to the radar look angle. Depending on their design and architecture, scatterometers utilize azimuth (fixed fan beam [7]), azimuth and polarization (pencil-beam [8]), or azimuth and incidence angle (rotating fan beam [9]) diversity to constrain a cost function for retrieving ocean vector winds. This cost function utilizes geophysical model functions (GMFs) such as CMOD7 for C-band scatterometers [10] to translate ocean vector winds, incidence angle, relative azimuth angle, and polarization into the NRCS metric. Synthetic aperture radar (SAR)—known for its high resolution and versatile imaging capabilities—can capture the

Manuscript received 1 March 2024; revised 8 May 2024; accepted 21 May 2024. Date of publication 30 May 2024; date of current version 11 June 2024. This work was supported in part by the National Key Research and Development Program, China under Grant 2023YFC2809102, in part by the Natural Science Foundation of China under Grant 41976174, and in part by the Pearl River Talent Recruitment Program under Grant 2019ZT08X751. *(Yuting Zhu and Giuseppe Grieco are contributed equally to this work.) (Yuting Zhu and Giuseppe Grieco are co-first authors.) (Corresponding author: Xiaoqing Wang.)*

Yuting Zhu and Jiarong Lin are with the School of Electronic and Communication Engineering, Sun Yat-Sen University, Shenzhen 510006, China (e-mail: zhuyt63@mail2.sysu.edu.cn; linjr9@mail2.sysu.edu.cn).

Giuseppe Grieco is with the Istituto di Scienze Marine—Consiglio Nazionale delle Ricerche (CNR-ISMAR), Calata Porta di Massa, 80133 Napoli, Italy (e-mail: giuseppe.grieco@cnr.it).

Marcos Portabella is with the Barcelona Expert Center, Institute of Marine Sciences (ICM-CSIC), 08003 Barcelona, Spain (e-mail: portabella@icm.csic.es).

Xiaoqing Wang is with the School of Electronic and Communication Engineering, Sun Yat-Sen University, Shenzhen 510006, China, and also with the Peng Cheng Laboratory, Shenzhen 518066, China (e-mail: wangxq58@mail.sysu.edu.cn).

Digital Object Identifier 10.1109/JSTARS.2024.3407115

© 2024 The Authors. This work is licensed under a Creative Commons Attribution-NonCommercial-NoDerivatives 4.0 License. For more information, see https://creativecommons.org/licenses/by-nc-nd/4.0/

surface roughness variations driven by atmospheric and oceanic processes. Advancements in SAR technology have enabled resolutions down to a few meters, rendering it exceptionally valuable in constrained marine settings. However, the single-antenna design of SAR limits its observational capacity regarding the look angle, which further complicates the application of GMFs for accurate predictions of wind vector. This challenge is frequently mitigated by integrating auxiliary wind direction data from additional SAR imagery, scatterometers, or numerical weather prediction (NWP) models [11]. Studies by Horstmann et al. [12] highlight a direct correlation between NRCS and wind direction, with notable errors in wind speed estimations occurring particularly at relative wind directions of [0,360] deg domain.

In SAR applications, wind field inversion is an ill-posed (underdetermined) problem, generally separated into wind speed and direction inversions. The most prevalent method for wind speed inversion employs collocated NWP model wind directions as inputs [13]. The wind speed is subsequently determined by inverting a GMF, which depends on the wind vector and on the polarization and frequency of the carrier signal. This approach, however, propagates any errors in wind direction input to the retrieved wind speed, heavily relying on the accuracy of the auxiliary wind direction data [14]. An essential aspect that warrants emphasis is the reliance of the SAR community on the GMF, which is originally developed for scatterometers. This GMF is tailored specifically to the mesoscale characteristics typical of scatterometer sensors, with both its theoretical scattering framework and empirical calibrations finely tuned for such applications. However, when this GMF is applied to SAR measurements, which often encompass different scales and dynamics, several theoretical and practical challenges arise. Despite its significance, this critical issue of transferring the scatterometer-optimized GMF to SAR contexts has been largely overlooked in the literature, yet it remains highly pertinent. Addressing this discrepancy is crucial for advancing the accuracy and applicability of SAR-derived measurements. Generally, SAR-derived wind speeds are of reasonable quality in open ocean settings away from meteorological disturbances, such as fronts or low-pressure areas [15], but they perform poorly in coastal zones where the models struggle to accurately capture the intricate small-scale dynamics.

Wind direction inversion techniques primarily rely on the information contained within the SAR image itself, utilizing both discrete and continuous methods. These include the Fourier transform [16], discrete wavelet transform [17], and local gradient analysis [18], [19], which employs the Sobel operator for numerical differentiation. However, these methodologies exhibit inherent limitations. Continuous wavelet transform techniques perform optimally under meteorological conditions characterized by weak divergence. In contrast, discrete wavelet transform, local gradient, and Fourier transform methods depend on the presence of wind-induced streaks on the sea surface, which are not consistently observable. Moreover, as previously noted, the accuracy of the retrieved wind speed is highly contingent on the precision of the ingested wind direction data. Notably, a 30° error in wind direction can lead to up to a 40% uncertainty in wind speed estimation. Recently, convolutional neural networks have been employed to deduce wind direction from SAR images, though this approach also necessitates auxiliary information to resolve the 180° ambiguity [20].

In 2002, Portabella et al. [14] introduced a sea-surface wind field inversion method grounded in Bayesian theory. This technique integrates the estimation of the SAR NRCS, the GMF model, prior data from NWP models, and their associated uncertainties. A variational formulation was developed to ascertain the optimal wind vector by minimizing the cost function. This method has demonstrated effectiveness across various datasets, including ERS-2, RADARSAT-1, Sentinel-1, and Gaofen-3 [21]. Consequently, derivative methods have been developed (e.g., the incorporation of Doppler frequency shifts into the Bayesian inversion scheme) to effectively improve the wind direction inversion [13], [22]. This underscores the capability of the Bayesian algorithm to probabilistically merge information from diverse sources, thereby augmenting wind field inversion through the cost function methodology. In this study, we introduce an additional element, azimuth cutoff information, into the Bayesian inversion scheme to improve the accuracy of sea-surface wind speed inversion.

Since its initial proposal by Kerbaol et al. [23], the azimuth cutoff information (λ) has been utilized to derive significant wave height (SWH) and ocean surface wind speed. Remarkably, it does not require data calibration or pre-existing wind direction information, which correspond to attributes that have recently led to its increased application. Although it has been demonstrated that azimuth cutoff can be used for wind speed inversion under completely developed sea conditions and across a wide range of wind speeds 5–25 m/s, and corresponding GMFs (λ_c-GMFs) have been developed linking (λ_c) with wind speed U and SWH [24], [25], this study aims to further harness the potential of azimuth cutoff. We introduce azimuth cutoff information as a new prior term in the Bayesian method, which consistently enhances the quality of wind speed retrieval. The effectiveness of this approach is discussed through the analysis of multisource data, including Sentinel-1 and Gaofen-3 satellite data, and the scatterometer onboard HY-2 A (i.e., HSCAT-A) and National Data Buoy Center (NDBC) buoy data as verification references.

The rest of this article is organized as follows. The datasets and data preprocessing used in this study are detailed in Section II. Thereafter, the theoretical foundation of the method is outlined in Section III, including the origins of the azimuth cutoff and the λ_c-GMF model, and explores how the azimuth cutoff information is integrated within the Bayesian inversion scheme. Section IV demonstrates the application of the method to multiple SAR images, accompanied by validation through scatterometer data and in situ buoy measurements. Finally, Section V concludes this article.

II. Data

The datasets consist of Sentinel-1 and Gaofen-3 SAR images, accompanied by wind data collocated from the European Centre for Medium-Range Weather Forecasts (ECMWF),

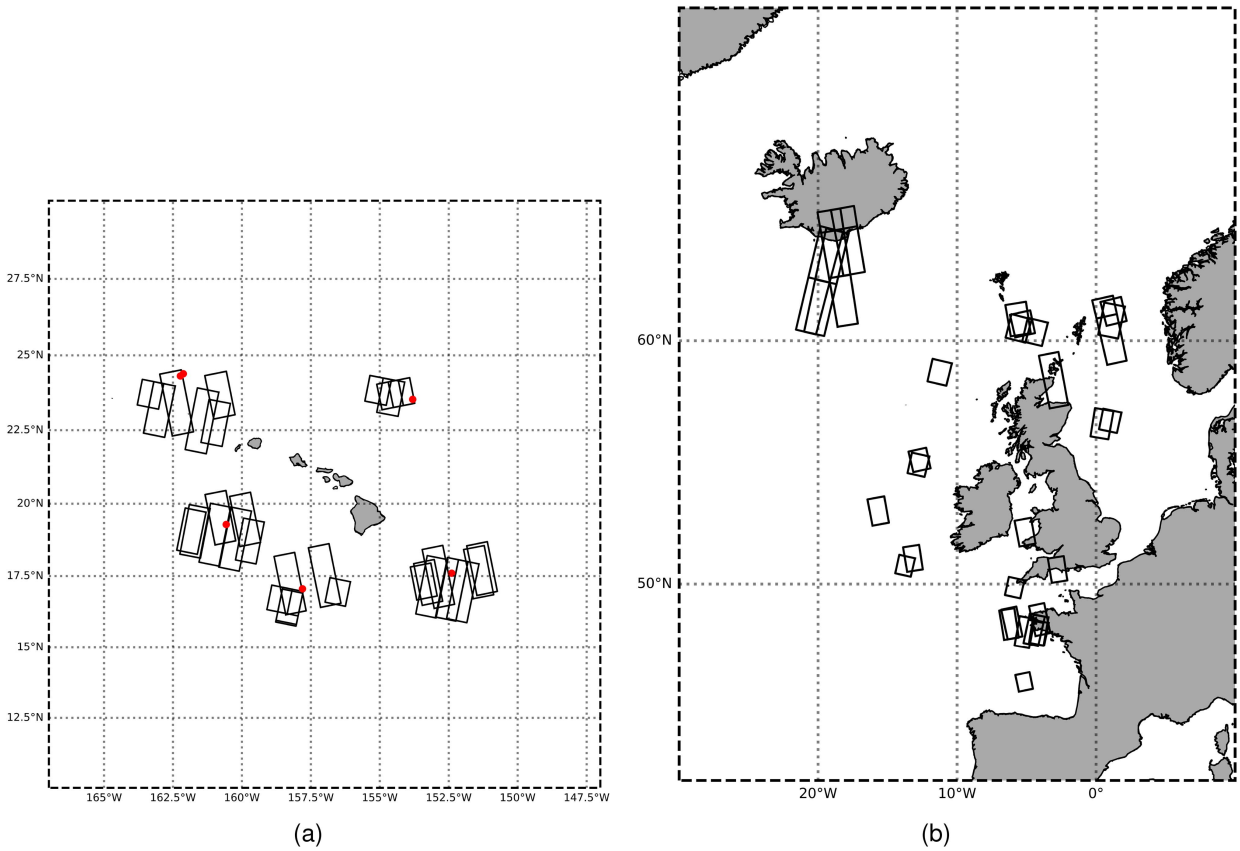

Fig. 1. Map of the image locations of the S-1 SAR acquisitions (black boxes) over the (a) Hawaiian Archipelago and (b) North-East Atlantic. Red points indicate the location of the NDBC buoys.

HSCAT-A scatterometer, and NDBC buoy wind database, although ECMWF winds are not used for verification purposes.

A. Sentinel-1 SAR Images

The Sentinel-1 dataset includes 99 ground range-detected (GRD) stripmap images captured in vertical polarization mode, with a pixel spacing of 10 m in both the range and azimuth directions. We extracted 1433 10×10 km^2 subimages collocated with HSCAT U measurements and ECMWF H_s. Sentinel-1 subimages are centered around HSCAT wind vector cell (WVC) grid point with acquisition times (S-1 and HSCAT) within 30 min. Among these, 58 images were acquired offshore from the Hawaii Archipelago, with the remaining 41 sourced over the Northeast Atlantic Ocean, as depicted in SAR image locations in Fig. 1. Table I in [24] provides detailed information on the dates and times of data acquisition to ensure the repeatability of the study. GRD products consist of focused SAR data that have been detected, multilooked, and projected onto the ground range. In this study, all Sentinel-1 SAR images were processed using the SNAP 9.0 platform for thermal noise removal and radiometric calibration.

B. Gaofen-3 SAR Images

The Gaofen-3 dataset comprises 11 quad-polarization strip (QPSII) mode images processed to yield Level-1 A single-look complex products. The pixel spacing was maintained at 25 m in both the range and azimuth directions. Among the four polarizations available, only the VV-type data were utilized in this study [21]. Table I offers a comprehensive account of the data acquisition times, incidence angle details, and corresponding buoy wind direction data. Adhering to the Gaofen-3 user manual, we implemented a series of preprocessing steps on the images, including radiometric calibration, multilooking, geometric correction, and noise filtering, utilizing the PIE-SAR software provided by the Aerospace Information Company.

C. ECMWF Reanalysis Data

The ECMWF model delivers globally gridded ocean surface wind vectors at a 10 m height and SWHs. In this study, we used ECMWF forecasts [ERA-interim (ERAi)] with a wind output resolution of 0.25° and SWHs at a 0.5° resolution, updated hourly. The ERAi data collocated with the sentinel data were derived through spatial and temporal interpolation of the initial data. We selected the ERAi grid point closest to each SAR WVC and temporally interpolated three different ERAi forecasts to coincide with the SAR imaging time. This global model data provides each SAR dataset with its own collocated data.

D. HSCAT-A Data

HSCAT-A data furnish retrieved ocean surface wind vectors at a 10 m height with a WVC size of 25×25 km. We utilized spatially collocated HSCAT-A measurements recorded within

TABLE I
COLLOCATED GAOFEN-3 SAR AND NDBC BUOY WIND DATA

Number	SAR mode	SAR time (UTC)	SAR incidence angle	Buoy name	Buoy latitude	Buoy longitude	Distance between SAR and Buoy (km)
1	QPSII	April 1, 2017 14:15	34.72	46 042	36.79	−122.47	2.2
2	QPSII	April 23, 2017 01:54	33.67	46 069	33.67	−120.2	0.7
3	QPSII	April 23, 2017 14:05	33.67	46 069	33.67	−120.2	2.8
4	QPSII	March 8, 2017 14:08:10	37.36	46 012	37.36	−122.88	2.3
5	QPSII	April 23, 2017 14:05	33.67	46 069	33.67	−120.2	6.3
6	QPSII	April 6, 2017 14:08	37.76	46 026	37.76	−122.84	5.1
7	QPSII	April 23, 2017 14:05	34.27	46 054	34.27	−120.46	7.6
8	QPSII	May 10, 2017 01:51	33.75	46 025	33.75	−119.05	3.9
9	QPSII	March 8, 2017 14:08:04	45.34	46 026	37.76	−122.84	4.4
10	QPSII	March 8, 2017 14:08:04	45.34	46 012	37.76	−122.88	5.9
11	QPSII	April 6, 2017 14:08:16	45.34	46 012	37.36	−122.88	2.8

30 min of the SAR acquisition instance. The wind speed consistency of HY-2 A with buoy winds was noted as ± 1.3 m/s [26].

E. NDBC Data

The NOAA NDBC buoy data provide in situ wind vectors. The buoy winds were measured using anemometers at different heights. Thus, all buoy wind speeds were first converted into 10-m-height winds using the methods in [27] before being used for comparison. All the SAR image WVC centers were within 10 km of the collocated buoy locations, and the time intervals between the collocated data points were within 30 min. NDBC measurements were delivered every hour with an accuracy of ± 1 m/s for wind speed (U), ± 0.2 m for SWH. Information about the buoy correspondence for the sentinel images can be found in Fig. 1(a) and for the Gaofen images in Table I.

III. THEORETICAL BACKGROUND AND METHODOLOGY

A. Azimuth Cutoff

The orbital motion of surface waves exerts a significant influence on the sea surface, as detected by the SAR system. This influence induces Doppler shifts that distort the phase history of the backscattered signal, which is essential for synthesizing azimuthal resolution. Consequently, SAR imaging tends to exhibit a low-pass effect, causing the ocean images to appear blurred in the azimuthal direction. This phenomenon is referred to as azimuth wavelength cutoff, or simply azimuth cutoff, which measures the effective SAR azimuth resolution [25].

Two principal phenomena contribute to azimuth cutoff. First, a scatterer moving with a radial velocity component v toward the radar will experience an azimuthal shift denoted as $\delta x = \beta v$, where β represents the range-to-platform velocity ratio. Thus, the deviations in the displacement of individual scatterers relative to the mean displacement of the SAR resolution cell create a "velocity spread" that smears the image of the resolution cell [28]. This effect, commonly known as velocity bunching, results in a cutoff wavelength strictly dependent on the velocity distribution of scatterers within the SAR resolution cell. This nonlinear modulation because of velocity bunching renders shorter waves in the azimuth direction undetectable in SAR imagery [29]. Second, scatterers possess a finite lifetime, referred to as the intrinsic scene coherence time. The coherence time of the ocean scene is typically shorter than the SAR acquisition time, which also leads to an intrinsic azimuth cutoff. Under the hypothesis of linear waves, λ_c can be expressed as follows:

$$\lambda_C(\theta,\phi_0) = \pi\xi' = \pi\frac{R(\theta)}{V}\sqrt{\int_0^\infty \omega^2 S(\boldsymbol{k}) F(\boldsymbol{k},\theta,\phi_0)\,\mathrm{d}\boldsymbol{k}} \tag{1}$$

$$F(\boldsymbol{k},\theta,\phi_0) = \cos^2(\theta) + \frac{\sin^2(\theta)}{2} + \Delta(\boldsymbol{k})\frac{\sin^2(\theta)}{4}\cos(2\phi_0) \tag{2}$$

where ω is the angular frequency of sea waves, $S(\boldsymbol{k})F(\boldsymbol{k},\theta,\phi_0)$ represents a factorized form of the sea wave spectrum. Here, F accounts for the dependency of the sea wave spectrum on the sea wavenumber k, the incidence angle θ, and the relative azimuth angle ϕ_0. In (1), S denotes the k-component of the wave spectrum, F represents the sea-surface wave spreading function, θ indicates the incidence angle, and ϕ is the relative direction of the ω-component of the wave spectrum. $R(\theta)$ symbolizes the range to the SAR platform, and V represents the SAR platform velocity modulus. ϕ_0 is defined as the wave direction relative to the range axis, with $\phi_0 = 0$ indicating the upwind direction. Each wave component contributes to the azimuth cut-off, and the relative azimuth angle should be considered for each component.

To retrieve λ_c from SAR imagery, some key steps are needed, as summarized in Fig. 2. As SAR images are larger than square

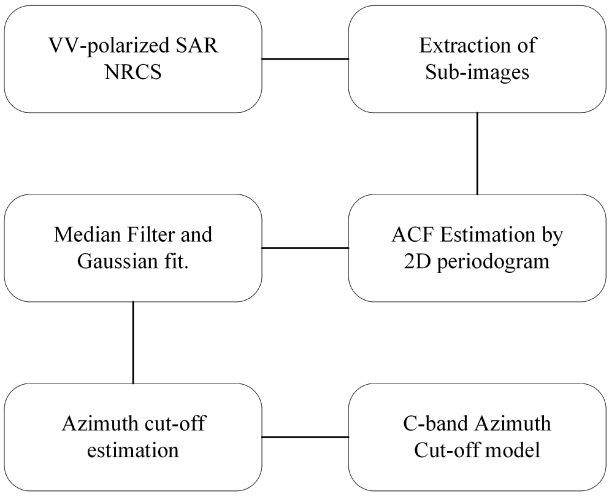

Fig. 2. Block scheme that depicts the main steps involved in the λ_C estimation. First, the SAR image is subdivided into subblocks, and the ACF is computed for each box through the IFFT of the obtained PSD. Next, a median filter is applied to obtain before the Gaussian fit is performed. Finally, the equation $\lambda_C = \sqrt{2\pi\sigma}$ is used.

imagettes of 10 km, they should be split into smaller boxes [30]. The first step involved partitioning the SAR imagery into sub-boxes. Subsequently, the power spectral density (PSD) was computed for each box. The third step involves estimating the autocorrelation function (ACF) by evaluating the inverse fast Fourier transform (IFFT) of the PSD. Subsequently, a median filter was applied to remove speckle noise peaks [31]. The above-mentioned approach is a spectral methodology and, here, the definition of ACF is used to estimate λ_c [32]. An alternative approach for evaluating the ACF is based on the cross-correlation function [33]. In this study, a PSD-based approach was adopted because it did not result in a loss of spatial resolution. In the last step, λ_c was estimated as follows:

$$\lambda_C = \sqrt{2\pi\sigma} \tag{3}$$

where σ represents the standard deviation of the Gaussian bell that optimally fits the estimated ACF. Intrinsically, the estimation of λ_c yields two identical values with opposite signs (refer to Fig. 3). Only the positive value is physically meaningful, as the negative value lacks physical relevance. An example demonstrating the azimuth cutoff and Gaussian fit is depicted in Fig. 3, where collocated SWH and wind speed U are noted in the legend. The typical sinc shape of the ACF is evident in scenarios involving azimuth-traveling waves, whereas this characteristic is nearly absent in range-traveling wave cases. The procedure of calculating λ_c across an entire SAR image by setting the size of the subimages (boxes) is described in Fig. 3, which was estimated as λ_c for a box, and then integrating all the estimated values. Additional information regarding the computation and calibration of the azimuth cutoff method is elaborated in [25]. The influence of ocean wind on azimuth cutoff is further explored in the subsequent section.

B. Relationship Between Azimuth Cutoff and Wind

Beal et al. [30] identified an empirical relationship between azimuth cutoff and the square root of SWH (H_s). Vachon et al. [19] noted a marginal empirical dependency of the azimuth cutoff on sea surface wind speed (U) at 10 m. Kerbaol et al. [23] similarly reported evidence of azimuth cutoff dependence on U. The derivation of U and H_s through SAR imagery using empirical functions is well-documented. The existing literature [34] analyzes this phenomenon, thereby confirming a linear relationship between the λ_c and U, emphasizing the interdependencies of wind speed and SWH. The proposed λ_c-GMFs in these studies reflect these relationships

$$\lambda_c = a + bU \tag{4}$$

$$\lambda_C^{20^\circ} = a + bU + c\sqrt{H_s} \tag{5}$$

$$\lambda_C^{20^\circ} = a + bU + c\left(H_s - H_s^{\mathrm{FD}}\right) \tag{6}$$

where a, b, and c are the model constants. $\lambda_C^{20^\circ}$ is a corrected value of λ_c. Indeed, it considers the dependency on the incidence angle. H_s^{FD} is the SWH in a fully developed sea state. The H_s^{FD} is calculated from the Pierson–Moskowitz spectrum following the equation:

$$H_{\mathrm{s}}^{\mathrm{FD}} \simeq 0.22\frac{U^2}{g} \tag{7}$$

where g is the Earth's acceleration. The fully developed sea state cases are identified with the following constraint:

$$\left|H_{\mathrm{s}} - H_{\mathrm{s}}^{\mathrm{FD}}\right| < 0.44\frac{U}{g}\Delta U \tag{8}$$

where $\Delta U = 1.3$ m/s is the agreement of HSCAT U with buoy measurements. Equations (4) and (5) were proposed by Beal et al. [30] and Vachon et al. [19], respectively. In our previous work [24], we introduced (6), which is an empirical formula that considers the impact of the incidence angle and depends on the development of the sea state.

In this study, we compiled a subset of λ_c values derived from the Sentinel-1 dataset images, along with the corresponding regional SWH and sea-surface wind speed. Fig. 4 presents a scatter plot of the wind speed and square root of H_s provided by ERAi against the filtered λ_c. The λ_c values exceeding 600 m were excluded, because longer waves are unlikely and cannot be detected with a defined box size of approximately 10 km. Fig. 4(a) displays the scatter plot of ERAi wind speed and the corresponding λ_c and $\lambda_c^{20^\circ}$ calculated for each region. Fig. 4(b) displays the wavelength cutoff versus the square root of H_s. For every figure, the top plots correspond to λ_c whereas the bottom plots correspond to $\lambda_c^{20^\circ}$.

It can be observed that, under all sea state conditions, the dependence of azimuth cutoff on SWH is approximately linear. However, the dependency of λ_c on wind speed is approximately linear only when the sea state is fully developed. Under the same wind conditions, the λ_c in the case of swells [i.e., the yellow markers in Fig. 4(a)] is larger than that during sea state growth [i.e., the blue markers in Fig. 4(a)]. Therefore, when using the empirical formula for azimuth cutoff, we chose (6), which

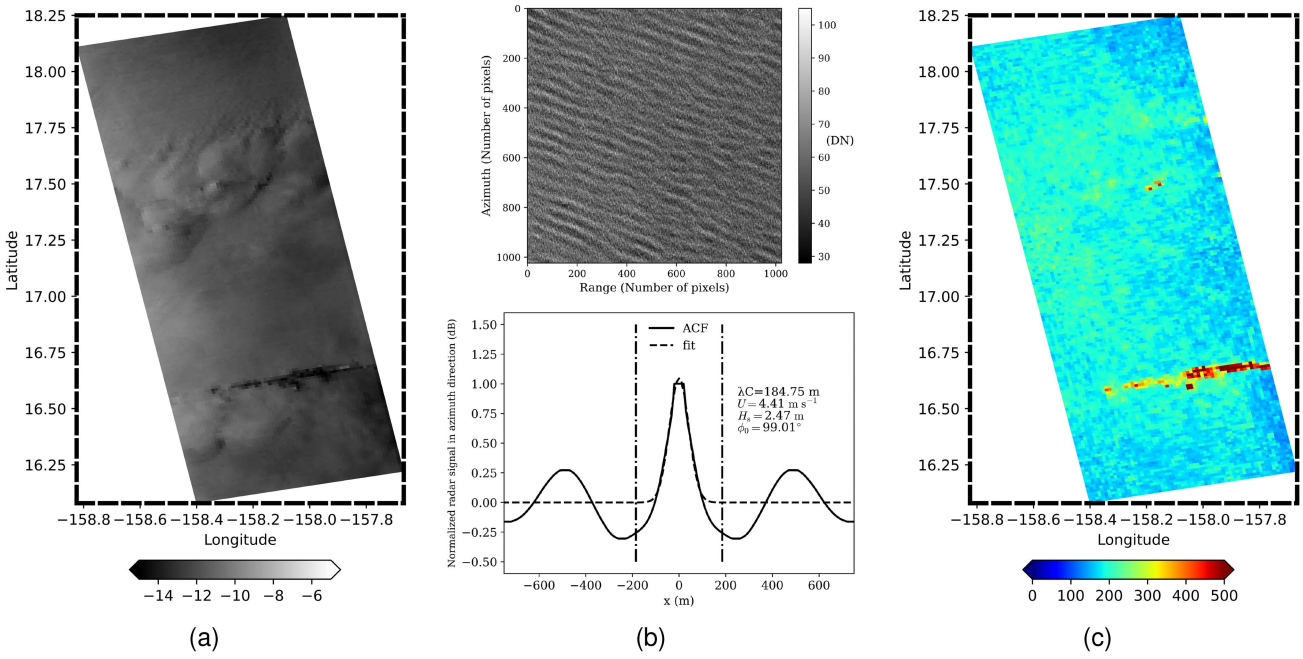

Fig. 3. Example of estimated λ_c from a Sentinel-1 SAR image. (a) VV-polarized NRCS image collected on November 11, 2014. (b) NRCS imagette of 1024 pixels extracted from (a). Bottom: azimuth ACF obtained with the inverse Fourier transform of the PSD of the NRCS imagette depicted in the top plot. (c) Estimated λ_c field from the entire Sentinel-1 SAR scene depicted in (a).

considers the development of the sea state. In the following section, we attempt to integrate the azimuth cutoff into the Bayesian method and discuss its implications.

C. Methodology

Portabella et al. [14] first proposed a methodology that combines SAR information with a priori information, considering that all sources of information, both observations and models, may contain errors. This method employs sea surface wind vectors from numerical weather forecasts, scatterometers, or other data sources as a priori (or background) information, denoted as u, and uses NRCS measurements from the SAR image as the observation state, represented as σ^0. Acknowledging the presence of errors in both u and σ^0, they formulated the following cost function:

$$J(u) = \underbrace{\left(\frac{\sigma^0 - \mathrm{CMOD}(u)}{\Delta\sigma^0}\right)^2}_{\text{NRCS term}} + \underbrace{\left(\frac{u - u_B}{\Delta u}\right)^2}_{\substack{\text{A priori}\\ \text{model term}}} \tag{9}$$

where the a priori wind vector is represented as u_B. $\Delta\sigma^0$ and Δu denote the Gaussian standard deviation errors for the NRCS and the model wind vector, respectively. Although the errors in the GMF CMOD and, notably, in the NWP are likely spatially correlated, they were not considered in this local (WVC-by-WVC) wind inversion scheme. Here, CMOD(u) refers to the CMOD7 GMF that relates the sea surface wind vector to the σ^0. The dependence on the incidence angle, antenna azimuth direction, and polarization is not explicitly indicated for brevity. Given that wind vector errors are presumed independent, u is broken down into its components (u_B, v_B) for analytical purposes

$$J(u) = \left(\frac{\sigma^o - \mathrm{CMOD}(u)}{\Delta\sigma^o}\right)^2 + \left(\frac{u_B - u}{\Delta u}\right)^2 + \left(\frac{v_B - v}{\Delta v}\right)^2 \tag{10}$$

where the last two terms are associated with background wind vector components (u_B, v_B). This method was extended to add the information contained in the azimuth cutoff. Simultaneous observations of NRCS (σ^0) and azimuth cutoff (λ_c) are assumed to be independent and related to the wind vector u by the CMOD and λ_c-GMFs, respectively. Following previous work [14], we assumed Gaussian errors for the observations, GMFs, and model information. This leads to a minimization problem for the determination of the maximum probability of getting a wind vector given (σ^0, λ_c)

$$J(\mathbf{u}) = \underbrace{\left(\frac{\sigma^0 - \mathrm{CMOD}(\mathbf{u})}{\Delta\sigma^0}\right)^2}_{\text{NRCS term}} + \underbrace{\left(\frac{\mathbf{u} - \mathbf{u}_B}{\Delta\mathbf{u}}\right)^2}_{\substack{\text{A priori}\\ \text{model term}}} + \underbrace{\left(\frac{\lambda_c - \lambda_C^{20^\circ}}{\Delta\lambda_c}\right)^2}_{\substack{\text{Azimuth cutoff}\\ \text{term}}} \tag{11}$$

where $\Delta\sigma^0$, $\Delta\lambda_c$, and Δu are the Gaussian standard deviation errors for the NRCS, the azimuth cutoff, and the model wind vector, respectively. We use (5) to calculate $\lambda_C^{20^\circ}$. The three parameter values are: $a = -90.33$, $b = 3.44$, and $c = 47.59$.

To explore the influence of each term within the cost function, we examined a hypothetical scenario featuring a "true" wind speed of 4.5 m/s and a direction of 105° (buoy wind vector). We assumed that the NWP model provided incorrect wind field information (speed: 8 m/s, direction: 285°). The terms of the cost function are computed and shown in Fig. 5, with wind components (u, v) ranging from -20 to 20 m/s. The reason

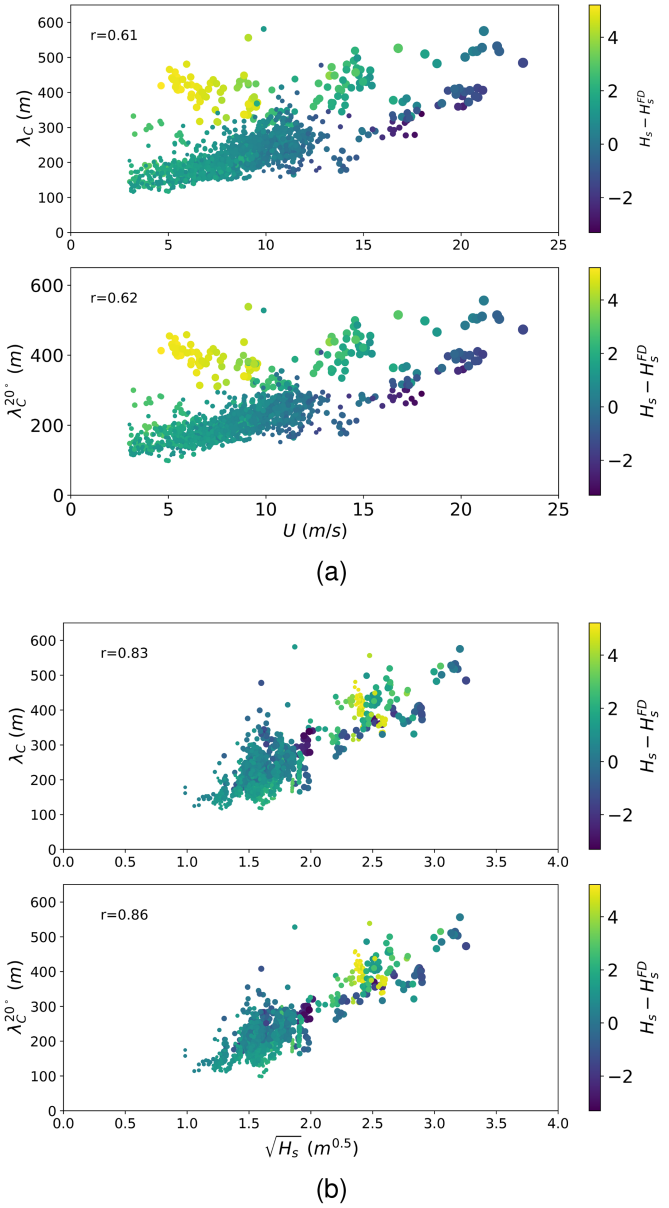

Fig. 4. Scatterplot analysis between λ_c against the square root of SWH and the wind speed before λ_c correction (above) and after (below). The color is proportional to the difference between H_s and H_s^{FD}. The two thresholds are calculated according to (8). r is the correlation coefficient between λ_c and U.

for setting the prior wind direction at 180° from the true wind direction was to verify the sensitivity of the azimuth cutoff to the wind direction. Also, we showed another theoretical case that the NWP model winds given (speed: 6 m/s, direction: 120°) is similar to the "true" winds.

The darker shading on the plots indicates lower values of the cost function, suggesting a higher likelihood of the wind vector representing the true wind conditions. The white crosses in Figs. 5 and 6 indicate the "true wind" conditions. The "NRCS term" and "azimuth cutoff term" are calculated using CMOD7 and λ_c-GMF, respectively. White squares indicate the results obtained after the minimization of the cost function. Figs. 5 and 6(a)–(c) illustrate the contributions of the NRCS, model wind vector, and azimuth cutoff terms, respectively, to the cost function. The addition of the model term [see Fig. 5(b) and 5(e)] accounts for both the wind speed and direction and their associated errors. When a priori information differs significantly from the true wind, this Bayesian approach does not compensate for this error. This is particularly relevant for the wind direction, since the observational term cannot constrain the wind direction [see the dark shading in Fig. 5(a) along the entire wind direction domain]. This was also demonstrated by Portabella et al. [14] and Mouche et al. [13]. As depicted in Fig. 5(c), relying solely on the azimuth cutoff would result in an underconstrained problem. However, as illustrated in Fig. 5(d), the NRCS and azimuth cutoff cost functions exhibit distinct profiles that complement each other, enhancing the overall resolution of the system. The aggregate cost function is presented in Fig. 5(f). Fig. 6 showcases a distinct theoretical scenario where the azimuthal term still lacks a constraining effect in wind inversion when the "true" and model wind vectors are closely aligned. Despite persisting direction ambiguities, the results displayed in Tables II and III illustrate how the inclusion of the azimuth cutoff term in the cost function significantly enhances the quality of wind speed retrievals.

TABLE II
COMPARISON OF RETRIEVAL VALUES ON INDIVIDUAL COST FUNCTIONS (SEE FIG. 5)

Retrieval cost term	Wind parameters	Retrieval result
(d)	Wind speed (m/s)	4.84
	Wind direction (°)	252
(e)	Wind speed (m/s)	6.12
	Wind direction (°)	289
(f)	Wind speed (m/s)	5.23
	Wind direction (°)	284

TABLE III
COMPARISON OF RETRIEVAL VALUES ON INDIVIDUAL COST FUNCTIONS (SEE FIG. 6)

Retrieval cost term	Wind parameters	Retrieval result
(d)	Wind speed (m/s)	4.84
	Wind direction (°)	252
(e)	Wind speed (m/s)	5.73
	Wind direction (°)	116
(f)	Wind speed (m/s)	5.02
	Wind direction (°)	114

IV. VALIDATION AND TESTING

A. Sentinel-1 Validation

1) Retrieved Wind Speed Quality: We evaluated the effectiveness of three distinct sea-surface wind retrieval methodologies by comparing their performance against HSCAT-A scatterometer data and NDBC buoy measurements. The evaluated algorithms include the conventional model using NWP wind directions coupled with CMOD7-derived wind speeds (hereafter referred to as the CMOD7 model), a Bayesian optimization approach (9), and the proposed novel method incorporating azimuth cutoff (11). Scatter plots displaying these comparisons use data points representing individual wind measurements derived from Sentinel-1 GRD data, collocated with both HSCAT-A and NDBC buoy wind data.

In the upper panels of Fig. 7 [i.e., Fig. 7(a)–(c)], the comparisons with HSCAT-A data reveal that the traditional CMOD7 model [see Fig. 7(a)] exhibits a significant bias of 1.55 m/s and

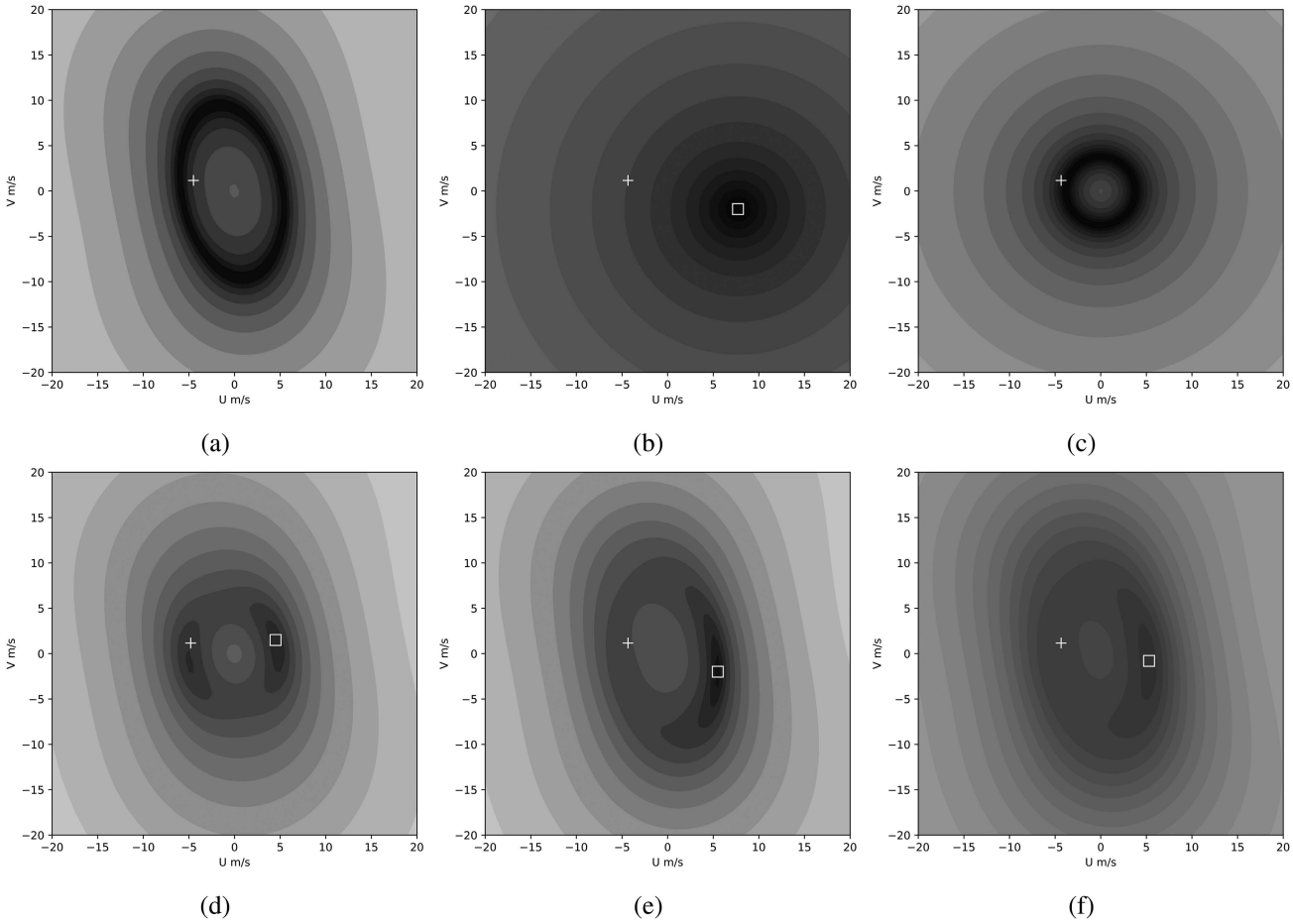

Fig. 5. Illustration of the terms of the cost function of (11) with respect to wind zonal (u) and meridional (v) components. We choose a model (a priori) wind of 8 m/s and direction of 285°. Darker shading indicates a lower value of the cost function terms and thus a higher likelihood of a solution being the true wind. (a) NRCS term. (b) Priori or background (model) term. (c) Azimuth cutoff term. (d) NRCS and azimuth cutoff terms. (e) NRCS and model term. (f) NRCS, model, and cutoff term. A white cross indicates the true wind situation, whereas the white squares indicate the local minima for cost function.

an RMSD of 3.03 m/s, indicating a notable discrepancy. The Bayesian optimization scheme [see Fig. 7(b)] and the proposed method [see Fig. 7(c)] demonstrate marked improvements, with biases close to zero (0.11 m/s and 0.02 m/s, respectively) and reduced RMSDs (2.32 m/s and 1.32 m/s, respectively), suggesting higher agreement with the HSCAT-A wind speeds. The panels of Fig. 8 [i.e., Fig. 8(a)–(c)] show the retrieval results against the NDBC buoy data. Similar to the HSCAT-A comparison, the CMOD7 model [see Fig. 8(d)] presents a higher bias (2.43 m/s) and an RMSD (3.27 m/s). The Bayesian optimization and the proposed method showed lower biases and RMSDs, although not as pronounced as in the HSCAT-A comparison.

Meanwhile, the figures presented [see Fig. 7(a)–(c)] illustrate the outcomes of wind speed inversion using three different methodologies under varying sea state conditions. Each figure uses color coding to represent the results from different sea states, where colors closer to yellow indicate data points under swell conditions, and deeper colors signify results from developing sea states.

For the CMOD7 method, there is a noticeable spread in the data points, particularly under swell conditions, indicating potential limitations in accurately capturing wind speeds during such sea states. The Bayesian approach shows an improvement in correlation and a reduction in RMSD compared to CMOD7, with a minimal bias of −0.11 m/s. This suggests that the Bayesian method is better at handling the variabilities and provides more accurate estimations under a wider range of conditions, including swells. Incorporating azimuth cutoff information significantly enhances the accuracy, as evidenced by the highest correlation and the lowest RMSD among the three methods. Notably, this method shows a substantial improvement in addressing the inaccuracies observed under swell conditions, which are better aligned with the reference wind speeds. The minimal bias of 0.02 m/s highlights the robustness of this method.

Overall, the proposed method significantly reduces the RMSD in comparison to both the CMOD7 and the optimized models, when assessed against HSCAT-A and buoy winds. This underscores the added value of incorporating the azimuth cutoff term in enhancing the quality of SAR retrieved wind speeds.

2) Retrieved Wind Direction Quality: This section of our study focuses on comparing the performances of sea-surface wind direction retrieval using three methodologies. Like the previous analysis, we evaluated the CMOD7 algorithm, Bayesian

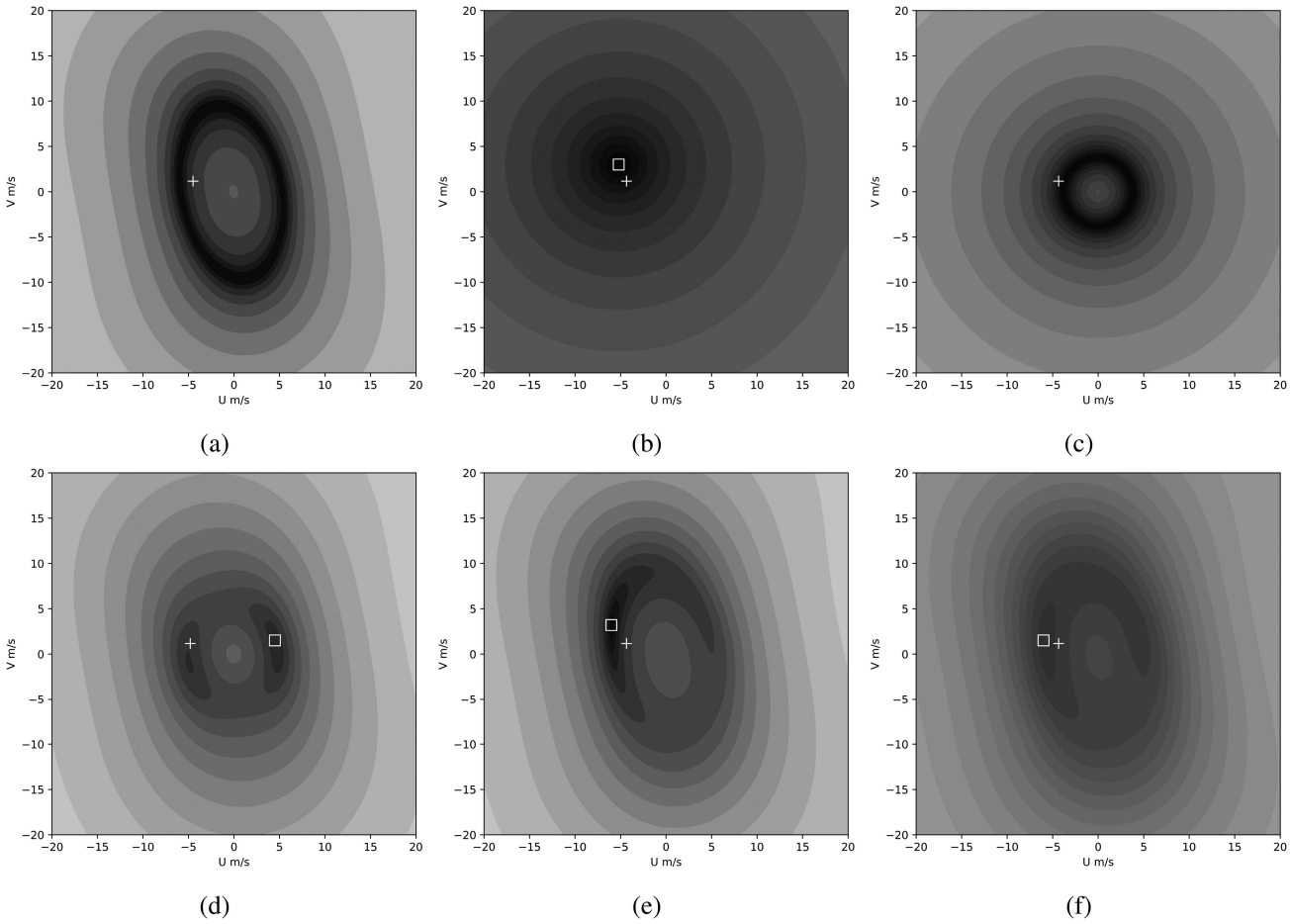

Fig. 6. Another example showing the terms of the cost function. We choose a model wind of 6 m/s and direction of 120°. (a) NRCS term. (b) A priori or background (model) term. (c) Azimuth cutoff term. (d) NRCS and azimuth cutoff terms. (e) NRCS and model term. (f) NRCS, model, and cutoff term.

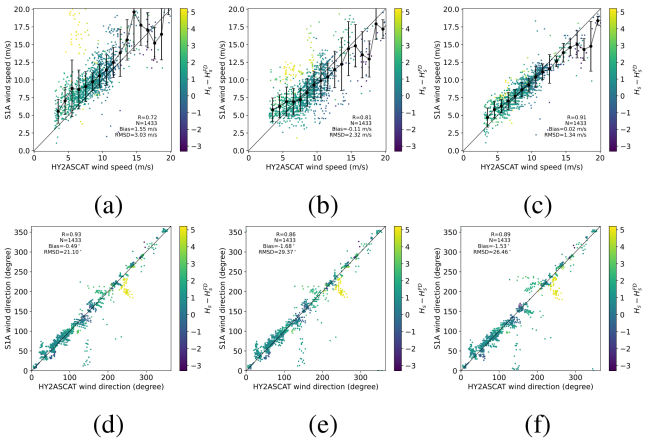

Fig. 7. Scatterplots of winds retrieved from the Sentinel-1 GRD data using (a) and (d) CMOD7, (b) and (e) optimal scheme, and (c) and (f) proposed scheme against the collocated HY2A-SCAT speeds (top) and wind directions (bottom). The colour is proportional to the difference between H_s and H_s^{FD}.

optimization approach, and a newly devised scheme. Scatter plots were used to compare our retrieval results with the HSCAT-A and NDBC buoy data.

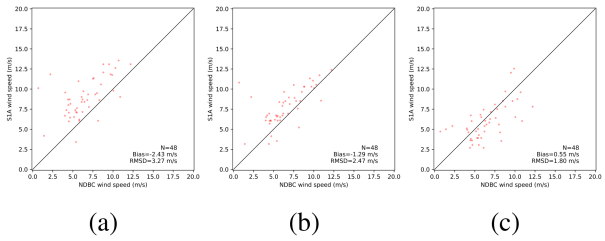

Fig. 8. Scatterplots of retrieved wind speeds from the Sentinel-1 GRD data using the (a) CMOD7, (b) optimal, and (c) proposed schemes against the collocated NDBC wind speeds.

In the panel, Fig. 7(d)–(f), the colors indicate the wind direction under varying sea state conditions. The CMOD7 method [see Fig. 7(d)], i.e., the ERAi wind directions, demonstrated a moderate correlation with HSCAT-A data ($R = 0.93$), albeit with a modest bias of 0.49° and an RMSD of 21.10°. Transitioning to the Bayesian optimization algorithm [see Fig. 7(e)] and the proposed scheme [see Fig. 7(f)], we observed a slight decline in correlation ($R = 0.86$ and $R = 0.89$, respectively) and an increase in both bias and RMSD, which indicates detrimental impact of these algorithms in the wind direction domain.

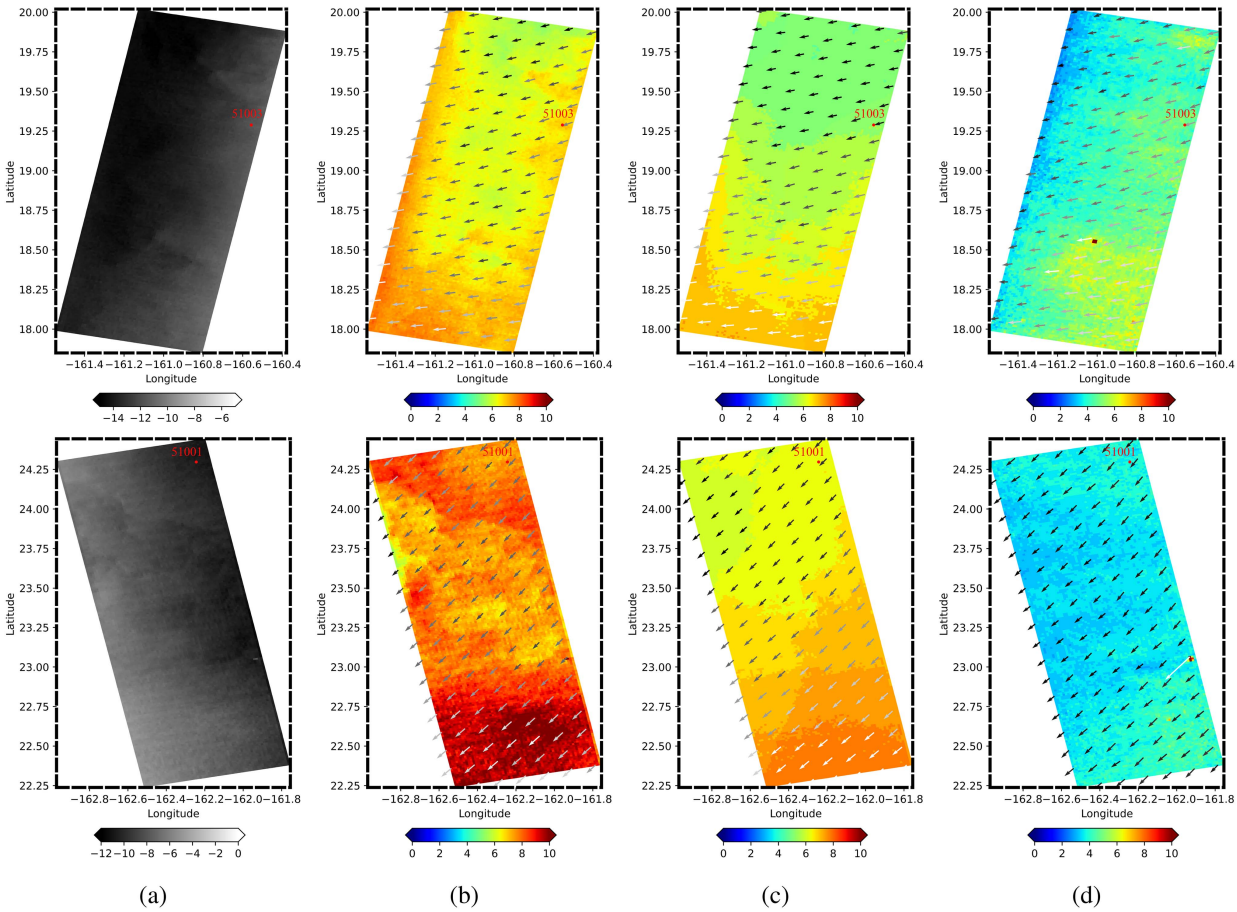

Fig. 9. Inverted Sentinel-1 wind map with different schemes. (a) VV-polarized NRCS SAR data acquired on April 12, 2015, at 16:40:32 UTC (top) and November 17, 2014, at 04:47:48 UTC (bottom). (b) Wind vectors retrieved from the CMOD7 scheme, (c) Wind vectors retrieved from the optimal scheme, and (d) Wind vectors retrieved from the proposed scheme.

Note that the azimuth cutoff information used in these methods demonstrates low sensitivity to wind direction, which outlines the lack of improvement in wind direction retrievals with the proposed method. Despite rigorous attempts to refine the retrieval process, its inherent insensitivity to azimuthal variation poses a significant challenge that merits further investigation.

3) Case Studies: The image depicted in Fig. 9 showcases two instances of Sentinel-SAR-derived wind maps, illustrating the inversion results for wind speed and direction using three different retrieval schemes. These results are compared against in situ measurements from buoys, which are marked by red dots at known geographic coordinates. The buoys selected for comparison exhibited similar wind speeds but notably different wind directions.

For Fig. 9 (upper), located at buoy 51 003 $(-160.57, 19.29)$, the CMOD scheme reported a wind speed retrieval of 7.22 m/s, closely aligning with the ERAi model (6.905 m/s) but higher than the buoy (5.4 m/s). The directions retrieved by all the schemes (note that that of the CMOD model actually corresponds to the ERAi direction by definition) were consistent with both the ERAi and buoy, showing excellent directional agreement. The optimal scheme reflected a modest underestimation in wind speed (6.57 m/s) compared to ERAi, while the proposed scheme retrieval of 5.024 m/s was closest to that of the buoy measurement, indicating a potential for enhanced accuracy in wind speed assessment. Looking at Fig. 9 (lower panels), at buoy 51 001 $(-162.23, 24.32)$, similar conclusions can be drawn. As shown in Table IV, the wind speed retrieved by the CMOD scheme was 7.539 m/s, which was again higher than that recorded by the buoy at 5.3 m/s. The retrievals of the optimal scheme (6.726 m/s) and the proposed scheme (4.724 m/s) were incrementally closer to the actual buoy measurements, notably the latter. In terms of wind direction, the CMOD and optimal schemes exhibited slight deviations from the ERAi and buoy data, whereas the retrieval of the proposed scheme was almost identical to that of the buoy.

Thus, based on this analysis, although the CMOD and optimal schemes tend to overestimate wind speed, the proposed scheme provided the most accurate wind speed retrievals when compared to buoy data. However, the advantage of wind direction accuracy for the proposed scheme was not as pronounced. Therefore, the proposed scheme may offer a more reliable alternative for wind speed estimation in operational applications, despite all methods displaying high fidelity in directional retrievals.

B. Gaofen-3 Buoy Validation

The wind retrieval data derived from 11 high-resolution Gaofen-3 SAR images demonstrate good agreement with in situ buoy wind speed measurements across all three considered

TABLE IV
LIST OF SAR WIND RETRIEVALS AND COLLOCATED NDBC BUOY 50 001 AND 50 003 DATA

		Fig 5. 51003 (–160.57, 19.29)			Fig 6. 51001 (–162.23, 24.32)		
Retrieval schemes	Wind parameters	Retrieval result	ECMWF	Buoy	Retrieval result	ECMWF	Buoy
CMOD scheme	Wind speed (m/s)	7.22	6.905	5.4	7.539	6.554	5.3
	Wind direction (○)	83.6	83.6	84	43.99	43.99	44
Optimal scheme	Wind speed (m/s)	6.57	6.905	5.4	6.726	6.554	5.3
	Wind direction (○)	81.2	83.6	84	39.80	43.99	44
Proposed scheme	Wind speed (m/s)	5.024	6.905	5.4	4.324	6.554	5.3
	Wind direction (○)	84.3	83.6	84	41.98	43.99	43

The winds are retrieved from Fig. 8 using the CMOD7, optimal, and proposed schemes.

TABLE V
COMPARISON OF DIFFERENT WIND SPEED AND DIRECTION ESTIMATION SCHEMES

Number	Buoy wind speed (m/s)	Buoy wind direction	CMOD7 speed (m/s)	CMOD7 direction	Optimal scheme speed (m/s)	Optimal scheme direction	Proposed scheme speed (m/s)	Proposed scheme direction
1	7.8	n/a	10.2	193	9.3	191	8.4	192
2	10.8	314	12.4	200	11.6	203	11.0	206
3	12.9	304	10.2	339	12.2	346	12.1	342
4	4.7	331	6.0	339	5.6	347	5.2	343
5	12.9	304	16.2	312	14.4	312	13.8	309
6	5.6	254	7.8	208	7.2	212	7.3	214
7	6.5	161	8.2	99	7.6	103	7.2	105
8	4.3	151	6.2	112	5.3	108	4.6	109
9	5.0	333	7.6	341	6.6	343	5.2	344
10	4.7	331	6.4	339	5.9	342	5.7	344
11	4.7	155	6.6	214	5.6	212	5.5	211

methodologies: the ERAi-based CMOD7 method, the optimal scheme, and the proposed scheme (referenced in Table V). However, as anticipated, the retrieved wind directions, heavily influenced by ERAi directions, exhibited more pronounced discrepancies when compared to buoy directions.

A detailed examination of the wind speed data revealed that all retrieval methods consistently estimated higher wind speeds than those recorded by the buoys. This discrepancy is typical in remote-sensing retrievals and can be attributed to the spatial and temporal differences between the point measurements of buoys and the area-averaged satellite observations. Notably, the proposed scheme tended to produce wind speed estimates that were closer to the buoy measurements, suggesting either a more refined calibration or an algorithm that is better attuned to capturing the nuances of ocean surface wind speeds. The CMOD7 method consistently overestimated wind speed compared to buoy data, with discrepancies ranging from 1.4 m/s to 3.3 m/s. Fig. 10 illustrates a retrieved wind map with all three approaches for case #8 in Table V, where the proposed method displays overall lower speeds than the other two methods. This finding is valid particularly for obtaining a closer approximation to the buoy wind speed, which suggests a refined calibration against in situ measurements.

However, wind direction retrieval presents a more complex scenario. The ERAi-based CMOD7 method showed significant deviations from the buoy-recorded wind directions, which in turn affected the performances of the other two schemes, as the Bayesian approaches are heavily constrained by the background (ERAi) wind direction. For instance, in cases where the ERAi direction deviated significantly from the buoy direction (e.g.,

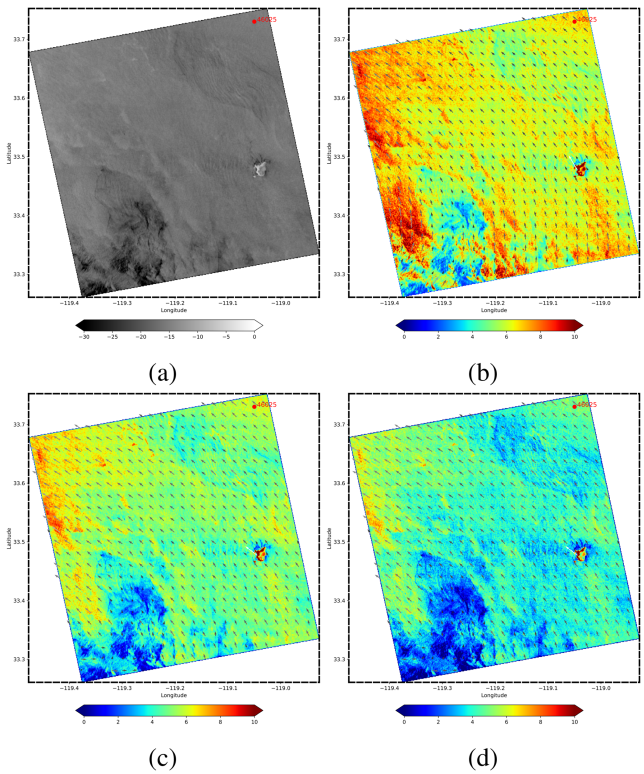

Fig. 10. Inverted Gaofen-3 wind map with different schemes. (a) QPSII VV-polarized NRCS data acquired on May 10, 2017, at 01:50:59 UTC. (b) Wind vectors retrieved from the CMOD7 scheme. (c) Wind vectors retrieved from the optimal scheme. (d) Wind vectors retrieved from the proposed scheme. Red dot represents the location of the collocated NDBC buoy 46 025. Both the background color and the arrow length represent the wind speed magnitude, and the arrow direction represents the wind direction.

case #7 in Table V, with a difference of more than 60°), the optimal and proposed schemes also exhibited notable errors.

Note that the fidelity of SAR-derived wind retrievals can be influenced by various factors, including the spatial resolution of the SAR imagery, atmospheric conditions at the time of SAR acquisition, and inherent limitations of the retrieval algorithms. Nevertheless, these preliminary results suggest that the proposed scheme can be further explored and refined for operational use, especially for wind speed retrieval in coastal and offshore environments, where accurate wind measurements are critical for maritime navigation and weather forecasting.

V. Conclusion

The application of scatterometer-optimized GMFs to SAR measurements introduces significant theoretical and practical challenges due to the differences in scale and dynamics between these sensors. This often-overlooked issue is crucial for refining SAR data accuracy and must be addressed to ensure reliable interpretations. In this study, we introduced a novel Bayesian wind field optimization inversion algorithm that effectively incorporates azimuth cutoff information into the inversion framework. The Bayesian approach facilitates the probabilistic fusion of data from diverse sources and enhances wind field inversion by integrating a cost function that effectively leverages azimuth cutoff data. The primary findings revealed that the azimuth cutoff demonstrates high sensitivity to wind speed and SWH, which establishes it as a crucial parameter for wind field retrieval across a range of sea-state conditions.

By adeptly utilizing azimuth cutoff information, our algorithm outperforms conventional methods, especially in lower wind speed regimes where accurate measurements are critical yet challenging to capture. The present methodology underwent rigorous evaluation against Sentinel-1 and Gaofen-3 SAR data, and the empirical results validated the effectiveness of the proposed method. The enhanced wind field inversion results of the algorithm were further demonstrated against scatterometer and in situ buoy data, demonstrating its practical applicability and reliability. In addition, we have validated the performance of various methods for wind speed inversion under different sea conditions. Our findings demonstrate that the Bayesian method, when integrated with azimuth cutoff information, consistently delivers superior results across diverse sea-states. This supports earlier recommendations [24] that combining azimuth cutoff with other wind inversion techniques can significantly improve the accuracy of wind speed estimates. We also examined the trend of inversion results relative to the distance from the coast. However, with only 287 coastal points among 1433 matched Sentinel data points, the dataset is inadequate for a meaningful analysis of azimuth cutoff in coastal regions. Despite this limitation, exploring coastal phenomena remains a highly promising and important area for future research, which we intend to continue developing.

In conclusion, the successful integration of azimuth cutoff information into the Bayesian inversion constitutes a significant advancement for SAR-based wind retrieval. This work supports the approach suggested by Valeria et al. [25], which advocates for the integration of azimuth cutoff information with other data to enhance the quality of wind speed retrieval. However, the present findings also indicate that while SAR-based retrieval methods have advanced in wind speed estimation, achieving similar improvements in wind direction remains inherently more challenging. Meanwhile, our study is currently limited by the insufficient collection of Gaofen-3 data, which impacts our ability to comprehensively compare two distinct types of datasets. Future research should focus on addressing these limitations.

Existing methods aimed at enhancing wind direction retrieval include integrating Doppler centroid information into the Bayesian method [13] and employing convolutional neural networks for wind direction detection [20]; however, these methods also exhibit certain limitations. Therefore, by more effectively constraining both wind speed (using azimuth cutoff information) and wind direction (through Doppler centroid and/or convolutional neural networks), this combined approach could substantially improve the quality of wind retrieval.

References

[1] R. M. Asiyabi, A. Ghorbanian, S. N. Tameh, M. Amani, S. Jin, and A. Mohammadzadeh, "Synthetic aperture radar (SAR) for ocean: A review," *IEEE J. Sel. Topics Appl. Earth Observ. Remote Sens.*, vol. 16, pp. 9106–9138, Aug. 2023.

[2] D. E. Weissman, D. B. King, and T. W. Thompson, "Relationship between hurricane surface winds and l-band radar backscatter from the sea surface," *J. Appl. Meteorol. Climatol.*, vol. 18, no. 8, pp. 1023–1034, 1979.

[3] F. Monaldo et al., "The SAR measurement of ocean surface winds: An overview," *ESA Spec. Publ.*, vol. 565, pp. 2–20, 2004.

[4] A. G. Fore, B. W. Stiles, P. T. Strub, and R. D. West, "QuikSCAT climatological data record: Land contamination flagging and correction," *Remote Sens.*, vol. 14, no. 10, pp. 2847–2850, 2022.

[5] G. Grieco, A. Stoffelen, A. Verhoef, J. Vogelzang, and M. Portabella, "Analysis of data-derived seawinds normalized radar cross-section noise," *Remote Sens.*, vol. 14, no. 21, pp. 5444–5458, 2022.

[6] J. Vogelzang and A. Stoffelen, "ASCAT land correction, report for the eumetsat ocean and sea ice saf," *Koninkl. Ned. Meteorol. Inst.*, 2020.

[7] J. Figa-Saldaña, J. J. Wilson, E. Attema, R. Gelsthorpe, M. R. Drinkwater, and A. Stoffelen, "The advanced scatterometer (ASCAT) on the meteorological operational (MetOp) platform: A follow on for European wind scatterometers," *Can. J. Remote Sens.*, vol. 28, no. 3, pp. 404–412, 2002.

[8] M. W. Spencer, C. Wu, and D. G. Long, "Tradeoffs in the design of a spaceborne scanning pencil beam scatterometer: Application to seawinds," *IEEE Trans. Geosci. Remote Sens.*, vol. 35, no. 1, pp. 115–126, Jan. 1997.

[9] Z. Li, A. Stoffelen, and A. Verhoef, "A generalized simulation capability for rotating-beam scatterometers," *Atmos. Meas. Techn.*, vol. 12, no. 7, pp. 3573–3594, 2019.

[10] A. Stoffelen, J. A. Verspeek, J. Vogelzang, and A. Verhoef, "The CMOD7 geophysical model function for ASCAT and ERS wind retrievals," *IEEE J. Sel. Topics Appl. Earth Observ. Remote Sens.*, vol. 10, no. 5, pp. 2123–2134, May 2017.

[11] G. K. Carvajal, L. E. Eriksson, and L. M. Ulander, "Retrieval and quality assessment of wind velocity vectors on the ocean with c-band SAR," *IEEE Trans. Geosci. Remote Sens.*, vol. 52, no. 5, pp. 2519–2537, May 2014.

[12] J. Horstmann, W. Koch, and S. Lehner, "Wind field retrieval using satellite based synthetic aperture radars," in *Proc. IEEE Int. Geosci. Remote Sens. Symp.*, 2000, pp. 1501–1503.

[13] A. A. Mouche et al., "On the use of doppler shift for sea surface wind retrieval from SAR," *IEEE Trans. Geosci. Remote Sens.*, vol. 50, no. 7, pp. 2901–2909, Jul. 2012.

[14] M. Portabella, A. Stoffelen, and J. A. Johannessen, "Toward an optimal inversion method for synthetic aperture radar wind retrieval," *J. Geophys. Res.: Oceans*, vol. 107, no. C8, pp. 1-1–1-13, 2002.

[15] W. Koch, "Directional analysis of SAR images aiming at wind direction," *IEEE Trans. Geosci. Remote Sens.*, vol. 42, no. 4, pp. 702–710, Apr. 2004.

[16] T. Gerling, "Structure of the surface wind field from the seasat SAR," *J. Geophys. Res.: Oceans*, vol. 91, no. C2, pp. 2308–2320, 1986.

[17] Y. Du, P. W. Vachon, and J. Wolfe, "Wind direction estimation from SAR images of the ocean using wavelet analysis," *Can. J. Remote Sens.*, vol. 28, no. 3, pp. 498–509, 2002.

[18] S. Zecchetto, "Wind direction extraction from SAR in coastal areas," *Remote Sens.*, vol. 10, no. 2, pp. 261–274, 2018.

[19] P. W. Vachon and F. Dobson, "Validation of wind vector retrieval from ERS-1 SAR images over the ocean," *Glob. Atmos. Ocean Syst.*, vol. 5, no. 2, pp. 177–187, 1996.
[20] A. Zanchetta and S. Zecchetto, "Wind direction retrieval from sentinel-1 SAR images using resnet," *Remote Sens. Environ.*, vol. 253, 2021, Art. no. 112178.
[21] L. Ren et al., "Assessments of ocean wind retrieval schemes used for Chinese Gaofen-3 synthetic aperture radar co-polarized data," *IEEE Trans. Geosci. Remote Sens.*, vol. 57, no. 9, pp. 7075–7085, Sep. 2019.
[22] J. Choisnard and S. Laroche, "Properties of variational data assimilation for synthetic aperture radar wind retrieval," *J. Geophys. Res.: Oceans*, vol. 113, no. C5, pp. 2–15, 2008.
[23] V. Kerbaol, B. Chapron, and P. W. Vachon, "Analysis of ERS-1/2 synthetic aperture radar wave mode imagettes," *J. Geophys. Res.: Oceans.*, vol. 103, no. C4, pp. 7833–7846, 1998.
[24] G. Grieco, W. Lin, M. Migliaccio, F. Nirchio, and M. Portabella, "Dependency of the sentinel-1 azimuth wavelength cut-off on significant wave height and wind speed," *Int. J. Remote Sens.*, vol. 37, no. 21, pp. 5086–5104, 2016.
[25] V. Corcione, G. Grieco, M. Portabella, F. Nunziata, and M. Migliaccio, "A novel azimuth cutoff implementation to retrieve sea surface wind speed from SAR imagery," *IEEE Trans. Geosci. Remote Sens.*, vol. 57, no. 6, pp. 3331–3340, Jun. 2019.
[26] J. Zhu, X. Dong, and R. Yun, "Calibration and validation of the HY-2 scatterometer backscatter measurements over ocean," in *Proc. IEEE Geosci. Remote Sens. Symp.*, 2014, pp. 4382–4385.
[27] S. D. Smith, "Coefficients for sea surface wind stress, heat flux, and wind profiles as a function of wind speed and temperature," *J. Geophys. Res.: Oceans*, vol. 93, no. C12, pp. 15467–15472, 1988.
[28] K. Hasselmann and S. Hasselmann, "On the nonlinear mapping of an ocean wave spectrum into a synthetic aperture radar image spectrum and its inversion," *J. Geophys. Res.: Oceans*, vol. 96, no. C6, pp. 10713–10729, 1991.
[29] W. Shao, Z. Zhang, X. Li, and H. Li, "Ocean wave parameters retrieval from sentinel-1 SAR imagery," *Remote Sens.*, vol. 8, no. 9, pp. 707–721, 2016.
[30] R. Beal, D. Tilley, and F. Monaldo, "Large-and small-scale spatial evolution of digitally processed ocean wave spectra from seasat synthetic aperture radar," *J. Geophys. Res.: Oceans*, vol. 88, no. C3, pp. 1761–1778, 1983.
[31] A. D. Goldfinger, "Estimation of spectra from speckled images," *IEEE Trans. Aerosp. Electron. Syst.*, vol. AES-18, no. 5, pp. 675–681, Sep. 1982.
[32] N. Wiener, "Generalized harmonic analysis," *Acta Math.*, vol. 55, no. 1, pp. 117–258, 1930.
[33] J. E. Stopa, F. Ardhuin, B. Chapron, and F. Collard, "Estimating wave orbital velocity through the azimuth cutoff from space-borne satellites," *J. Geophys. Res.: Oceans*, vol. 120, no. 11, pp. 7616–7634, 2015.
[34] W. J. Donnelly et al., "Revised ocean backscatter models at c and ku band under high-wind conditions," *J. Geophys. Res.: Oceans*, vol. 104, no. C5, pp. 11485–11497, 1999.

Yuting Zhu was born in Anhui Province, China, in 1995. He received the B.S. degree in electronic science and technology from the School of Hainan University, Haikou, China, in 2017. He is currently working toward the Ph.D. degree in winds and currents retrieval with the School of Electronics and Communication, Sun Yat-Sen University, Shenzheng, China.

He has been with the Institute of Industrial Science (IIS), The University of Tokyo, Tokyo, Japan, since February 2024. His research interests include ocean microwave remote sensing and SAR signal processing.

Giuseppe Grieco received the M.Sc. degree in marine sciences from the University Parthenope of Napoli, Naples, Italy, in 2001, and the Ph.D. degree in environmental engineering from the Università della Basilicata, Potenza, Italy, in 2008.

he has been with the Istituto di Scienze Marine, Consiglio Nazionale delle Ricerche (ISMAR-CNR), Venice, Italy, since 2021. Since 2014, his main scientific interests are related to the estimation of the sea state and the wind field from active microwave sensors, namely scatterometers, Synthetic Aperture Radars (SARs), and GNSS-Reflectometry. He carried out this activity with the Agenzia Spaziale Italiana (ASI), Rome, Italy, the Royal Netherlands Meteorological Institute (KNMI), De Bilt, The Netherlands, and the Institute of Marine Sciences, Spanish National Research Council (ICM-CSIC), Madrid, Spain, and currently with ISMAR-CNR. In the past, he was involved in scientific activities aimed at retrieving the thermodynamic state of the atmosphere and some minor and trace gases tropospheric concentration from infrared hyperspectral measurements.

Jiarong Lin was born in Guangdong Province, China, in 2000. He received the B.S. degree in electronic information science and technology in 2022 from Sun Yat-Sen University, Shenzhen, China, where he is currently working toward the M.Sc. degree in SAR data processing with the School of Electronics and Communication.

His research interests include SAR signal processing and radar processing.

Marcos Portabella was born in Barcelona, Spain, in 1970. He received the B.Sc. degree in physics from the University of Barcelona, Barcelona, Spain, in 1994, the M.Sc. degree in remote sensing from the Institute of Space Studies of Catalonia, Barcelona, Spain, in 1995, and the Ph.D. degree in physics from the University of Barcelona in 2002.

He is with the Institut de Ciencias del Mar, Barcelona, Spain, where he is involved in satellite remote sensing, particularly scatterometry, SAR, and *L*-band radiometry.

Xiaoqing Wang was born in Jiangxi Province, China, in 1978. He received the B.S. degree in electronic engineering from Xiamen University, Xiamen, China, in 2000 and the Ph.D. degree in signal processing from the University of Chinese Academy of Sciences, Beijing, China, in 2005.

From 2005 to 2016, he was an Assistant Researcher and an Associate Researcher with the Institute of Electronics, Chinese Academy of Sciences. From 2016 to 2019, he was an Associate Researcher and Researcher with the Institute of Microelectronics, Chinese Academy of Sciences. Since 2019, he has been a Professor with the School of Electronics and Communication, Sun Yat-Sen University, Shenzhen, China. His research interests include ocean microwave remote sensing, SAR signal processing, and radar processing.